

A systematic study on the aromatic and aliphatic hydrocarbon emission features of nearby galaxies using AKARI near-IR spectra

Tsubasa KONDO,^{1,*} Hidehiro KANEDA,¹ Shinki OYABU,² Takuma KOKUSHO,¹ Toyooki SUZUKI,³ Risako KATAYAMA,¹ Eiko KOZAKI,¹ Itsuka YACHI,¹ Keita YOSHIDA,¹ and Shohei ONO¹

¹Graduate School of Science, Nagoya University, Furo-cho, Chikusa-ku, Nagoya, Aichi 464-8602, Japan

²Institute of Liberal Arts and Sciences, Tokushima University, 1-1 Minami-josanjima-cho, Tokushima-shi, Tokushima, 770-8502, Japan

³Institute of Space and Astronautical Science, Japan Aerospace Exploration Agency, 3-1-1 Yoshinodai, Chuo-ku, Sagami-hara, Kanagawa 252-5210, Japan

*E-mail: t.kondo@u.phys.nagoya-u.ac.jp

ORCID: 0009-0002-5486-0068

Abstract

Interstellar hydrocarbon dust containing aromatic and aliphatic hydrocarbons, like polycyclic aromatic hydrocarbons (PAHs), is believed to be processed by various factors including UV radiation fields and mechanical shocks in the galactic environments. We systematically investigate the processing of hydrocarbon dust, especially the likely causes for the variations of the luminosity ratio of aliphatic to aromatic hydrocarbon emission features, using the near-infrared (IR) spectral features at wavelengths 3.3 μm and 3.4–3.6 μm observed with AKARI/IRC. We analyzed 243 near-IR spectra of 240 star-forming (ultra-)luminous IR galaxies (the total IR luminosity, $L_{\text{IR}} > 10^{11} L_{\odot}$), 119 spectra of 105 star-forming IR galaxies ($10^{10} L_{\odot} < L_{\text{IR}} < 10^{11} L_{\odot}$), and 94 spectra of 65 sub-IR galaxies ($L_{\text{IR}} < 10^{10} L_{\odot}$), in addition to 232 spectra of 36 Galactic H II regions as a reference sample. We performed near-IR spectral model fitting to estimate the luminosities of the aromatic and aliphatic hydrocarbon features and the H I recombination line Br α . The result indicates that the luminosity ratios of the aliphatic to the aromatic hydrocarbons ($L_{\text{aliphatic}}/L_{\text{aromatic}}$) in the sample galaxies show considerably large variations, compared to those in the Galactic H II regions, $L_{\text{aliphatic}}/L_{\text{aromatic}}$ systematically decreasing with L_{IR} and $L_{\text{Br}\alpha}$. We find that (sub-)IR galaxies with continuum colors bluer at 4 μm tend to have higher $L_{\text{aliphatic}}/L_{\text{aromatic}}$, which is likely to reflect the intrinsic nature of PAHs outside the H II region where the PAHs remain non-processed by strong UV radiation fields. We also find that some ultra-luminous IR galaxies with continuum colors redder at 4 μm show extremely low $L_{\text{aliphatic}}/L_{\text{aromatic}}$, which is likely to be caused by blending aliphatic emission and absorption features due to the presence of an obscured galactic nucleus in merger systems.

Keywords: galaxies: ISM—galaxies: star formation—infrared: galaxies—ISM: lines and bands

1 Introduction

Polycyclic aromatic hydrocarbons (PAHs) are believed to be likely carriers of the so-called unidentified infrared emission bands, whose spectral features are observed in a wide range of wavelengths in the near- to mid-infrared (IR) regions. Among them, representative ones are observed at wavelengths of 3.3, 6.2, 7.7, 8.6, 11.3, 12.7, and 17 μm (e.g., Draine & Li 2007; Li 2020). For example, the aromatic hydrocarbon feature at 3.3 μm is ascribed to a C-H stretching mode (e.g., Draine 2011). At wavelengths of 3.4–3.6 μm contiguous to the aromatic hydrocarbon feature at 3.3 μm , there are sub-features produced by C-H stretching modes of aliphatic hydrocarbons (e.g., Kwok 2007). Those features, especially the aromatic ones, have so far been detected from various kinds of objects including reflection nebulae, young stellar objects, Galactic H II regions, Galactic photo-dissociation regions, and external galaxies including not only star-forming but also quiescent galaxies (e.g., Peeters et al. 2002; Kaneda et al. 2008; Yamagishi et al. 2012; Mori et al. 2014).

Several studies have reported that the processing of hydrocarbon dust is likely to be caused by various interstellar environ-

mental factors such as radiation field intensity and radiation hardness (e.g., Galliano et al. 2008; Tielens 2008; Hemachandra et al. 2015; Lai et al. 2023). For example, in M 82, a nearby starburst galaxy, it is shown that the relative abundance of aliphatic hydrocarbons is higher in the halo region than in the galactic center region, suggesting that mechanical shocks by galactic superwinds may have shattered large carbonaceous grains to produce small aliphatic hydrocarbons (Yamagishi et al. 2012). On the other hand, in Galactic H II regions, the ratio of the aliphatic to the aromatic hydrocarbon intensity decreases with the PAH ionization degree which is affected by the UV radiation field. This is likely to reflect the fact that aliphatic hydrocarbons are more fragile than aromatic hydrocarbons for photodissociation (Mori et al. 2014). Similarly to Galactic H II regions, in luminous infrared galaxies (LIRGs) and ultra-luminous infrared galaxies (ULIRGs), the ratio of the aliphatic to the aromatic hydrocarbon luminosity decreases with the interstellar radiation field (ISRF) strength (Kondo et al. 2024). In addition to the ISRF strength, galaxy mergers with strong shocks may cause a further decrease in the ratio of the aliphatic to the aromatic hydrocarbons (Kondo et al. 2024).

As for recent observations of JWST, in extragalactic H II re-

gions of nearby star-forming galaxies (NGC 628, NGC 1365, NGC 7496, and IC 5332), Egorov et al. (2023) show that the ratio of fluxes in JWST bands, $(F_{F770W} + F_{F1130W})/F_{F2100W}$, tracing the mass fraction of PAHs to the total dust, decreases with the ionization parameter of the H II regions, suggesting that the extreme-UV radiation (> 13.6 eV) destroys PAHs efficiently. In addition, the JWST observation of the nearby galaxy, NGC 7469, reveals that the ratio of the aliphatic to the aromatic hydrocarbon intensity decreases with $[\text{Ne III}]/[\text{Ne II}]$ that represents the hardness of the radiation field. This result indicates that the harder radiation fields destroy aliphatic hydrocarbons more efficiently than aromatic hydrocarbons (Lai et al. 2023). From a systematic study of galaxies at redshift $z \sim 0.2\text{--}0.5$ observed with JWST NIRCam, Lyu et al. (2025) show that the ratio of the aliphatic to the aromatic hydrocarbons decreases with the star formation rate (SFR) indicators (L_{IR} , L_{aromatic} , and spectral-energy-distribution-based SFR), but not with the redshift, stellar mass, metallicity, or morphology.

Organic matter like PAHs is thought to evolve with changes in the molecular structure due to various kinds of processing in the interstellar environments (e.g., Berné & Tielens 2012). However, it is yet to be clarified how aromatic and aliphatic hydrocarbons are processed in various kinds of the interstellar environments of galaxies. In this study, systematically analyzing the near-IR spectra of the nearby galaxies observed by AKARI/IRC (Infrared Camera; Murakami et al. 2007; Onaka et al. 2007), we investigate how the luminosity ratio of the aliphatic to the aromatic hydrocarbons changes depending on the surrounding interstellar environments, and how the relationship between the ratio of the aliphatic to the aromatic hydrocarbons and the interstellar environments can be linked to the evolution of the organic matter.

2 Observations

2.1 Spectroscopy with AKARI/IRC and data reduction

The AKARI/IRC (Onaka et al. 2007) spectroscopic observations of nearby galaxies were carried out in the director's time program (DT), in the AKARI mission programs (MP) of AGNUL, AMUSE, EGANS, FUHYU, ISMGN, MSAGN, MSFGO, QSONG, and SPICY, and in the AKARI open time programs (OT) of ABCGA, ASCSG, BRFSR, CLNSL, COABS, GOALS, H2BCG, H2IRC, HOTCO, ISBEG, NISIG, NULIZ, SHARP, and SYDUS. The AKARI telescope and instruments were cooled by mechanical coolers and liquid helium (Murakami et al. 2007). We call the observation periods before and after the boil-off of the liquid helium Phase 2 and Phase 3, respectively. In our paper, we use the spectroscopic data of nearby galaxies retrieved from DARTS¹. The spectral data were obtained by using the NG mode of the near-IR channel of IRC (2.5–5.0 μm) in Phases 2 and 3 (Ohyama et al. 2007). We extracted spectral data from the slit (Ns or Nh) or the window (Np) as designated in the AOT parameter.

For the data reduction, we basically used the official AKARI data reduction pipeline for Phases 2 and 3 (IRC Spectroscopy Toolkit Version 20181203 and IRC Spectroscopy Toolkit for Phase 3 data Version 20181203)². Since the temperature of the detector increased to ~ 40 K in Phase 3, the number of hot pixels in the detector array increased, and accordingly the quality of the spectral data deteriorated. Therefore, in addition to the official AKARI data reduction pipeline, we applied custom procedures to

all the spectral data taken in Phase 3 in order to remove the effect of the hot pixels and to improve the signal-to-noise (S/N) ratios (Yamagishi et al. 2011). Finally, we combined spectral data with the same target coordinates (RA, Dec) and the same AOT parameters. We selected nearby galaxies with redshift, $z < 0.4$, since we focus on the 3.3 μm aromatic hydrocarbon feature and the 3.4–3.6 μm aliphatic hydrocarbon sub-features which are covered by AKARI/IRC near-IR spectroscopy. As a result, we newly analyzed 699 spectra of 623 nearby galaxies, in addition to the sample of Kondo et al. (2024), for the present study.

2.2 Classification and selection of galaxies

We classify the sample galaxies into four luminosity classes based on the total infrared luminosity, L_{IR} : (1) sub-infrared galaxies (sub-IRGs; $L_{\text{IR}} < 10^{10} L_{\odot}$), (2) infrared galaxies (IRGs; $10^{10} L_{\odot} < L_{\text{IR}} < 10^{11} L_{\odot}$), (3) luminous infrared galaxies (LIRGs; $10^{11} L_{\odot} < L_{\text{IR}} < 10^{12} L_{\odot}$), and (4) ultra-luminous infrared galaxies (ULIRGs; $L_{\text{IR}} > 10^{12} L_{\odot}$). L_{IR} is estimated from spectral energy distribution (SED) fitting, which is described in Section 4. When it is difficult to estimate L_{IR} due to insufficient SED data points, we define the luminosity class of our sample galaxy referring to the information in the NASA/IPAC Extragalactic Database (NED)³ and also that in previous studies for several galaxies (Sanders & Mirabel 1996; Engelbracht et al. 2004; Kennicutt et al. 2011; Suzuki et al. 2013; Zhang et al. 2014; Persic & Rephaeli 2019; Persic et al. 2024).

We also classify the sample galaxies into three galaxy types based on the equivalent width of the 3.3 μm aromatic hydrocarbon feature, EW_{aromatic} , and the near-IR continuum slope, Γ ($F_{\text{cont}} \propto \lambda^{\Gamma}$ for the wavelength ranges of 2.55–2.70 and 3.60–4.00 μm), as adopted in Imanishi et al. (2010) and Kondo et al. (2024): (1) pure star-forming galaxies (SFGs; $EW_{\text{aromatic}} > 40$ nm and $\Gamma < 1$), (2) SF-AGN (active galactic nucleus) composite galaxies ($EW_{\text{aromatic}} > 40$ nm and $\Gamma > 1$), and (3) AGN-dominated galaxies ($EW_{\text{aromatic}} < 40$ nm and $\Gamma > 1$). It should be noted, however, that this galaxy type classification method using near-IR spectra may misclassify, for example, compact obscured nuclei as pure SFGs because EW_{aromatic} of such AGNs can be as large as those of pure SFGs (e.g., García-Bernete et al. 2025). On the other hand, since the classification of sub-IRGs with EW_{aromatic} and Γ is not straightforward because of the significant contribution of stellar components to the near-IR continuum in such IR-inactive galaxies, we treat all sub-IRGs as one group. As a result of this classification for the 623 nearby galaxies, we identify 216 pure star-forming (U)(L)IRGs and 103 sub-IRGs, on which we focus in this paper. AGN-inclusive (U)(L)IRGs are treated separately in Katayama et al. (2025).

To estimate the fluxes of the hydrocarbon features, we carry out spectral model fitting, and then we select the spectra mainly based on the χ^2 statistics for the full-range model fitting (section 3.1) and/or the local-range (2.65–3.70 μm) model fitting (section 3.2) with the threshold of $\chi^2_{\nu} \leq 2.0$. Since artifacts due to the data reduction and the instrumental errors tend to appear near the edges of the wavelength range of 2.5–5.0 μm , we limit the fitting range to 2.55–4.85 μm to avoid the influence of those artifacts. We find that the official AKARI data reduction pipeline produces unreasonably small or large spectral errors for the observed flux densities in some cases. Therefore, if necessary, we adjust error values by scaling them so that the error values are consistent with the standard deviation of the differential values between adjacent

¹ <https://darts.isas.jaxa.jp/en>

² <https://www.ir.isas.jaxa.jp/AKARI/Observation/support/IRC/>

³ <https://ned.ipac.caltech.edu/>

Table 1. Classification of the sample galaxies for the present study, based on the equivalent width of the 3.3 μm aromatic hydrocarbon feature, EW_{aromatic} , and the near-IR continuum slope, Γ .

Sample	Star-forming	Composite	AGN	Others	Kondo et al. (2024)	Total
ULIRG	32	N/A	N/A	N/A	52	84
LIRG	85	N/A	N/A	N/A	71	156
IRG	94	N/A	N/A	N/A	11	105
sub-IRG	21	2	2	38	2	65

Table 2. Initial values and the range of the parameters in the model fitting.

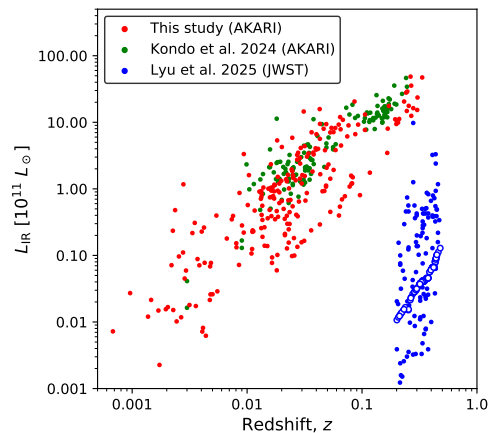
Feature	Central wavelength [μm]	Feature width (Ns)	Feature width (Nh)	Feature width (Np)	Relative intensity
Aromatic	3.29 (3.26–3.32)	0.014 (0.012–0.035)	0.014 (0.012–0.035)	0.014 (0.012–0.035)	–
Aliphatic 1	3.41 (3.39–3.44)	0.030 (0.01–0.1)	0.030 (0.01–0.1)	0.030 (0.01–0.1)	–
Aliphatic 2	3.46 (3.44–3.49)	0.031 (0.025–0.050)	0.025 (0.020–0.050)	0.034 (0.030–0.050)	–
Aliphatic 3	3.51 (3.49–3.53)	0.031 (0.025–0.050)	0.025 (0.020–0.050)	0.034 (0.030–0.050)	–
Aliphatic 4	3.56 (3.53–3.59)	0.031 (0.025–0.050)	0.025 (0.020–0.050)	0.034 (0.030–0.050)	–
H I Br β	2.62 (2.59–2.65)	0.031 (0.025–0.035)	0.025 (0.020–0.030)	0.034 (0.030–0.040)	0.571
H I Pf12	2.76 (2.73–2.79)	0.031 (0.025–0.035)	0.025 (0.020–0.030)	0.034 (0.030–0.040)	0.040
H I Pf η	2.88 (2.85–2.91)	0.031 (0.025–0.035)	0.025 (0.020–0.030)	0.034 (0.030–0.040)	0.050
H I Pf ϵ	3.04 (3.01–3.07)	0.031 (0.025–0.035)	0.025 (0.020–0.030)	0.034 (0.030–0.040)	0.067
H I Pf δ	3.30	0.031 (0.025–0.035)	0.025 (0.020–0.030)	0.034 (0.030–0.040)	0.093
H I Pf γ	3.74 (3.71–3.77)	0.031 (0.025–0.035)	0.025 (0.020–0.030)	0.034 (0.030–0.040)	0.134
H ₂ S(13)	3.85 (3.82–3.88)	0.031 (0.025–0.035)	0.025 (0.020–0.030)	0.034 (0.030–0.040)	–
H I Hu15	3.91 (3.88–3.94)	0.031 (0.025–0.035)	0.025 (0.020–0.030)	0.034 (0.030–0.040)	0.012
H I Br α	4.05 (4.02–4.08)	0.031 (0.025–0.035)	0.025 (0.020–0.030)	0.034 (0.030–0.040)	1.000
H I Hu13	4.18 (4.15–4.21)	0.031 (0.025–0.035)	0.025 (0.020–0.030)	0.034 (0.030–0.040)	0.019
He I	4.30 (4.27–4.33)	0.031 (0.025–0.035)	0.025 (0.020–0.030)	0.034 (0.030–0.040)	–
H I Hu12	4.38 (4.35–4.41)	0.031 (0.025–0.035)	0.025 (0.020–0.030)	0.034 (0.030–0.040)	0.024
H I Pf β	4.65 (4.62–4.68)	0.031 (0.025–0.035)	0.025 (0.020–0.030)	0.034 (0.030–0.040)	0.202
H ₂ O ice	3.05 (2.90–3.10)	0.13 (0.05–1.0)	0.13 (0.05–1.0)	0.13 (0.05–1.0)	–
CO ₂ ice	4.27 (4.22–4.32)	0.15 (0.05–1.0)	0.15 (0.05–1.0)	0.15 (0.05–1.0)	–
CO ice or gas	4.67 (4.62–4.72)	0.15 (0.05–1.0)	0.15 (0.05–1.0)	0.15 (0.05–1.0)	–

residual data points from the spectral fitting model in the wavelength ranges of 2.6–3.05 and 3.65–4.85 μm where spectral features are relatively free, and then carry out spectral fitting again.

For relatively faint spectra which show flux densities at 3.6–3.7 μm less than 5.0 mJy and EW_{aromatic} less than 40 nm, where the detection of PAHs is susceptible to artifacts, we apply tight criteria using the result of the full-range model fitting (section 3.1) to select the spectra that are relatively unaffected by artifacts. We also select galaxies with χ^2_{ν} for the local-range model fitting less than 2.0. We add 30 spectra to the sample, which are rejected in the above data selection but significantly show strong hydrocarbon features without any apparent systematic residuals from the fitting model in the wavelength regions of 2.6–3.05 and 3.65–4.85 μm .

As a result, we obtain 228 spectra of 211 pure star-forming (U)(L)IRGs and 92 spectra of 63 sub-IRGs. Besides, we add the sample of Kondo et al. (2024) which consists of 134 spectra of 134 pure star-forming (U)(L)IRGs and 2 spectra of 2 sub-IRGs. In addition, we re-analyze the 232 spectra of the 36 Galactic H II regions presented in Mori et al. (2014) as a reference sample. The statistics of the sample galaxies are summarized in table 1. In figure 1, the distribution of L_{IR} as a function of redshift, z , for the sample galaxies in this study is compared with those of the AKARI sample in Kondo et al. (2024) and the FRESCO sample observed with JWST/NIRCam WFSS (Lyu et al. 2025). The sample galaxies in this study span a wide range of L_{IR} at $z < 0.3$, which are systematically fainter than those in Kondo et al. (2024) and complementary to the FRESCO sample that covers much lower lumi-

nosities with a similarly broad L_{IR} range at $z > 0.2$.

**Fig. 1.** Comparison of L_{IR} and redshift, z , for the AKARI sample galaxies in this study (red circles), those in Kondo et al. (2024) (green circles), and the JWST FRESCO sample galaxies in Lyu et al. (2025) (blue circles), where open marks represent galaxies with L_{IR} upper limits. Alt text: One scatter plot.

3 Spectral fitting

3.1 Full-range model fitting

In order to exclude spectra with relatively large systematic errors in addition to evaluating errors in the spectra and correcting them if necessary, we first carry out a model fitting to the spectra in the wavelength range of 2.55–4.85 μm , and then select the spectral data reliable for further analyses of hydrocarbon features (section 3.2). The fitting model used here is given by

$$F_\nu = e^{-(\tau_{\text{H}_2\text{O}} + \tau_{\text{CO}_2} + \tau_{\text{CO}})} (F_{\text{cont}} + F_{\text{aromatic}} + F_{\text{aliphatic}} + F_{\text{recomb}}), \quad (1)$$

where $\tau_{\text{H}_2\text{O}}$, τ_{CO_2} , τ_{CO} , F_{cont} , F_{aromatic} , $F_{\text{aliphatic}}$, and F_{recomb} are the optical depths due to H_2O ice, CO_2 ice, and CO ice or gas, the flux densities of the continuum, the aromatic hydrocarbon feature at 3.3 μm , the aliphatic hydrocarbon sub-features at 3.4–3.6 μm , and the H I and He I recombination lines, respectively. For F_{cont} , we use a polynomial function of the 4th or 5th order depending on the result of an F -test with a 90% confidence level. For F_{aromatic} , we use the following Drude profile (Draine & Li 2007):

$$F_{\text{aromatic}} = \frac{a_r b_r^2}{\left(\frac{\lambda}{\lambda_r} - \frac{\lambda_r}{\lambda}\right)^2 + b_r^2}, \quad (2)$$

where a_r and b_r are the peak of the feature profile and the FWHM divided by λ_r , the central wavelength of the feature profile, respectively.

The aliphatic hydrocarbon features at 3.4–3.6 μm are considered to be composed of several components. Here we assume four representative components (e.g., Sloan et al. 1997, Kwok 2011), while Mori et al. (2014) assumed two components. Following Kondo et al. (2024), we apply a Lorentzian profile for the 3.41 μm feature and Gaussian profiles for the 3.46, 3.51, and 3.56 μm features. Since the H I and He I recombination emission lines are not spectrally resolved with the Ns or Nh slits or the Np window, we use Gaussian profiles to fit the emission lines. For the wavelength range of 2.55–4.85 μm , we consider the 13 recombination lines listed in table 2:

$$F_{\text{recomb}} = \sum_{i=1}^{13} \alpha_i \exp \left[-4 \ln 2 \frac{(\lambda - \lambda_{r,i})^2}{\gamma^2} \right], \quad (3)$$

where α , γ , and λ_r are the Gaussian profile peak, the FWHM, and the central wavelength, respectively. Finally, we use Gaussian profiles to fit the absorption features due to H_2O ice, CO_2 ice, and CO ice or gas, following Shimonishi et al. (2010):

$$\tau_{\text{H}_2\text{O}} + \tau_{\text{CO}_2} + \tau_{\text{CO}} = \sum_{i=1}^3 \alpha_i \exp \left[-4 \ln 2 \frac{(\lambda - \lambda_{r,i})^2}{\gamma^2} \right]. \quad (4)$$

In fitting the spectral data with the model, we divide the fitting procedure into three steps and determine the fitting parameters step by step. First, we carry out model fitting to determine the parameters of the continuum for the wavelength ranges of 2.55–2.60, 2.65–2.70, 3.60–3.70, 3.80–4.00, 4.10–4.20, 4.35–4.45, and 4.80–4.85 μm , which are free of the hydrocarbon features, the H I and He I recombination lines, and the ice absorption features. Secondly, we determine parameters for the hydrocarbon features, the H I and He I recombination lines, and the ice absorption features, while the parameters of the continuum determined in the first fitting step are fixed. Finally, we fine-tune the amplitudes of the absorption features and all the emission features and lines under the condition that the continuum parameters and the shape parameters of the features and the lines (i.e., the feature and line

widths, the central wavelength) are fixed at the values determined in the first and second fitting steps. We also fix the relative strengths of the four aliphatic components at those determined in the second step (i.e., the overall profile of the aliphatic feature. Here we confirm that the aliphatic flux error thus estimated is comparable to the sum of the observed flux density errors for the 3.4–3.6 μm excess above the underlying continuum (the former-to-latter ratio of $1.3^{+0.9}_{-0.1}$ on average), and thus reasonable or at least not underestimated. We adopt such initial values and limited fitting ranges of the parameters as listed in table 2. The ranges of the amplitudes of the H I recombination lines are constrained within a factor of 2 with respect to the values predicted in the Case B condition ($T = 10^4$ K, $n_e = 10^3$ cm^{-3}) on the basis of the $\text{Br}\alpha$ line strength (Hummer & Storey 1987, see table 2) except the $\text{Pf}\delta$ line whose amplitude is fixed at the value predicted in the Case B condition, since the amplitude of the $\text{Pf}\delta$ line cannot be determined due to blending with the aromatic hydrocarbon feature at 3.3 μm .

Based on the result of the model fitting, we evaluate a χ^2 divided by the number of spectral data points (χ^2) over the wavelength ranges of 2.6–3.05 and 3.65–4.85 μm , and then select the spectral data with the threshold of $\chi^2 \leq 2.0$ to exclude spectra with relatively large systematic deviations from the fitting model due to artifacts. In some cases, spectral data show an unusually broad feature over the wavelength range of 3.05–3.2 μm , which is likely a fake feature, but not a real hydrocarbon feature; we exclude the spectra that show the ratio of the integrated flux over the wavelength range of 3.05–3.2 μm to the aromatic hydrocarbon feature at 3.3 μm higher than 1/3. An example is shown in figure 2, where a broad excess is seen at 3.1–3.2 μm with an FWHM of approximately 0.1 μm . The only known feature or line around this wavelength range is H_2 1–0 O(5) at 3.235 μm . However, since this excess is significantly broader than the spectral resolution of AKARI/IRC, it is likely to be a fake feature. Through this spectral fitting, we calculate the luminosities of the aromatic hydrocarbon emission feature (L_{aromatic}), aliphatic hydrocarbon emission features ($L_{\text{aliphatic}}$), and the H I recombination line $\text{Br}\alpha$ ($L_{\text{Br}\alpha}$).

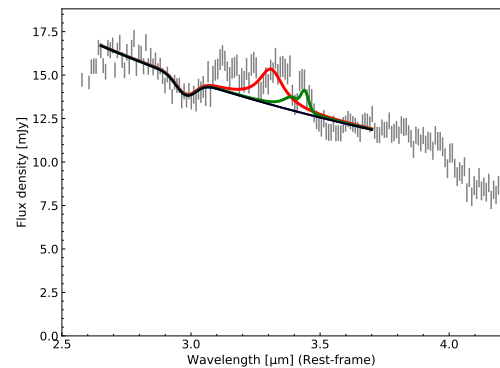


Fig. 2. Example spectrum showing an unusually broad feature over the wavelength range of 3.1–3.2 μm . The black, red, and green lines represent the near-IR continuum, the 3.3 μm aromatic feature, and the 3.4–3.6 μm aliphatic feature, respectively. Alt text: One example spectrum observed with AKARI/IRC.

3.2 Local-range model fitting

The full-range fitting model may have uncertainties in determining the shape of the underlying continuum below the aromatic

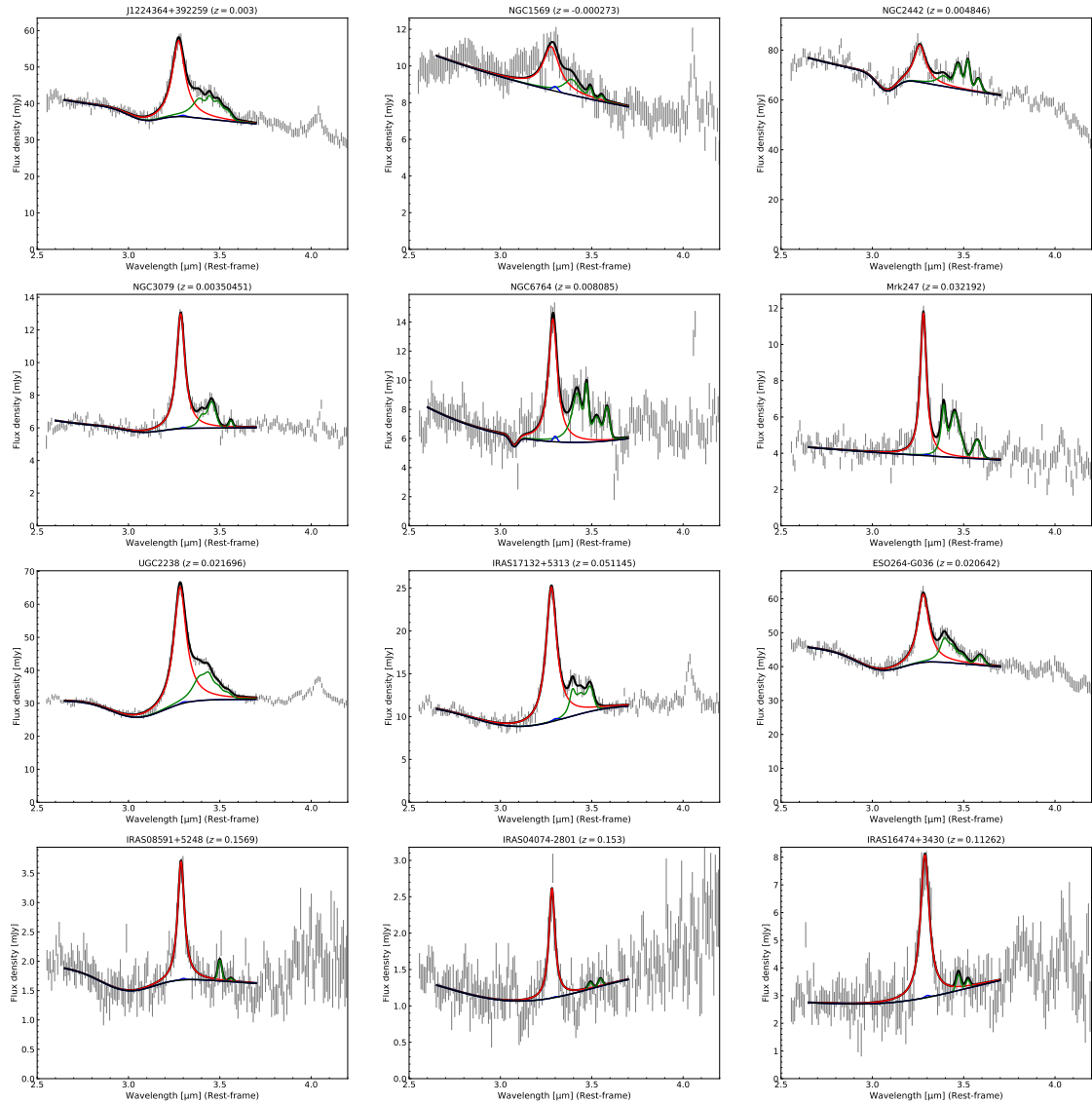


Fig. 3. Examples of the near-IR spectral fitting using the local-range model. The spectral model is composed of the near-IR continuum (black line), aromatic hydrocarbon emission feature (red line), aliphatic hydrocarbon emission features (green lines), and H I Pf δ recombination line (blue line). The hydrocarbon features and Pf δ recombination line are attenuated by the H₂O ice absorption. Alt text: Twelve panels of examples for near-infrared spectral fitting.

and aliphatic features, because it is difficult to uniquely determine the full-range continuum with a single model. Those features are quite broad, while the Br α line is narrow but its flux estimation is somewhat affected by the presence of the CO₂ absorption feature. Therefore, for the purpose of estimating the fluxes of the aromatic and aliphatic features more robustly, we perform local-range model fitting for the spectra with the corrected errors. Following Kondo et al. (2024), we use a power-law ($F_{\text{cont}} \propto \lambda^\Gamma$, where Γ is a free parameter) as a continuum model to determine the local-range continuum for the hydrocarbon features in the wavelength ranges of 2.55–2.60, 2.65–2.70, 3.60–3.70, and 3.80–4.00 μm . On the other hand, since it is difficult to reproduce the local-range continuum using a power-law model when the hot dust emission is relatively strong, we also test the following model:

$$F_{\text{cont}} = C_1 \lambda^\Gamma + C_2 \frac{B_\nu(\lambda, T)}{\lambda^2}, \quad (5)$$

where C_1 , C_2 are the amplitudes of the power-law and the modified blackbody model, respectively. Based on the result of an

F -test with a 90% confidence level, we adopt the power-law or the second model as a continuum model for the local-range fitting. The fitting models for the aromatic hydrocarbon feature, the aliphatic hydrocarbon features, the H I recombination line Pf δ , and the H₂O ice absorption feature are the same as those used in the full-range fitting model, while the results of the full-range fitting are used as initial input values. Figure 3 shows examples of the result for the near-IR spectral model fitting with the local-range model. Through this spectral fitting, we calculate L_{aromatic} and $L_{\text{aliphatic}}$, which are adopted in the following results and discussions.

4 Spectral energy distribution fitting

We perform model fitting to the spectral energy distributions (SEDs) which are composed of near- to far-IR photometric data obtained with AKARI (AKARI All-Sky Survey: IRC Point Source

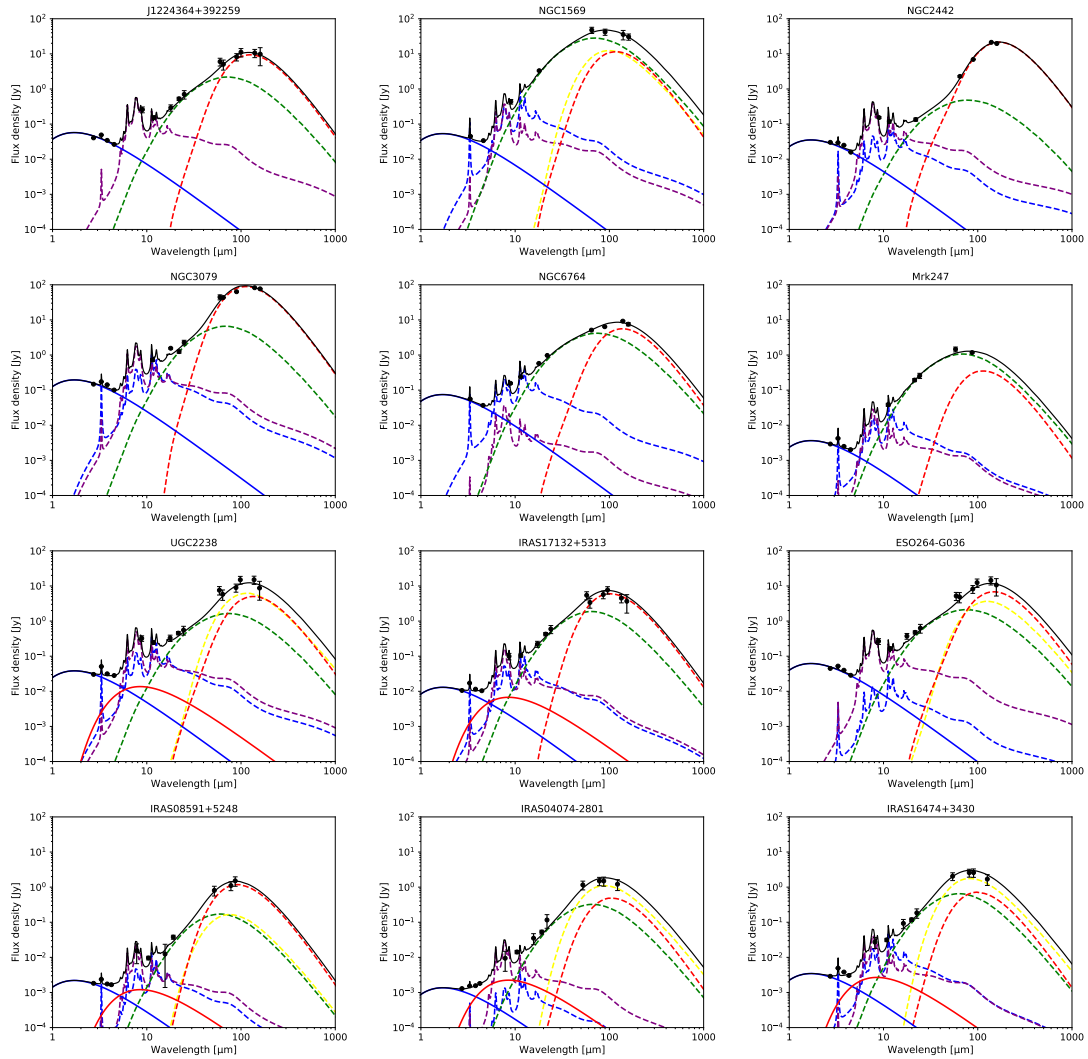


Fig. 4. Examples of the SED fitting to the same galaxies as shown in figure 3. The SED model is composed of stellar continuum (blue solid line), hot dust continuum (red solid line), ionized PAHs (purple dashed line), neutral PAHs (blue dashed line), small amorphous carbon (green dashed line), large amorphous carbon (yellow dashed line), and amorphous silicate dust (red dashed line). Alt text: Twelve panels of examples for spectral energy distribution fitting.

Catalogue Version 1.0; Ishihara et al. 2010, AKARI All-Sky Survey: FIS Bright Source Catalogue Version 2.0, AKARI Far-infrared All-Sky Survey Maps; Doi et al. 2015), WISE (WISE All-sky Source Catalog; Wright et al. 2010), and IRAS (IRAS Faint Source Catalog v2.0; Moshir et al. 1990). Based on the AKARI spectroscopic observation coordinates, the one-to-one source cross-matching is performed for each point source catalog independently with the following search radius: 1.5 arcmin for AKARI/IRC, FIS, WISE and 3.3 arcmin for IRAS, where we do not consider any possible nearby source contamination. In addition to the photometric data, we add to the SEDs four near-IR data points by binning the AKARI near-IR spectra for the wavelength ranges of 2.55–2.90, 3.20–3.38, 3.60–4.00, and 4.10–4.90 μm , following the procedure in Kondo et al. (2024).

We use an SED model based on DustEM (Compiegne et al. 2011) which consists of the following three dust components: PAHs, amorphous carbon (amC), and amorphous silicate (aSil). PAHs are composed of neutral and ionized PAHs. We fit the SEDs of the sample galaxies on the condition that the abundance ratio of the neutral to ionized PAHs is free. The amC is divided into

large amC (LamC) and small amC (SamC) components based on the dust size. Furthermore, we add two blackbody models with temperatures of 600 and 3000 K, which represent a hot dust and a stellar continuum, respectively. Finally, we perform the SED fitting to the 411 sample galaxies which have more photometric data points than the number of the free parameters of the SED model. Figure 4 shows examples of the SED fitting results. We estimate the hot dust continuum luminosities, L_{hot} , the stellar continuum luminosities, L_{star} , and the total IR luminosities, $L_{\text{IR}} (= L_{\text{star}} + L_{\text{hot}} + L_{\text{PAH}} + L_{\text{amC}} + L_{\text{aSil}})$, of the sample galaxies, which are integrated over the wavelength range of 1–1000 μm .

5 Result

As a result of the near-IR spectral fitting, 428 of the 456 spectra of all the sample galaxies show detection of the aromatic hydrocarbon feature at 3.3 μm with $S/N > 3$, the breakdown of which is 239 for (U)LIRGs, 117 for IRGs, and 72 for sub-IRGs. Figure 5 shows correlation plots between L_{aromatic} , $L_{\text{aliphatic}}$, and $L_{\text{Br}\alpha}$ es-

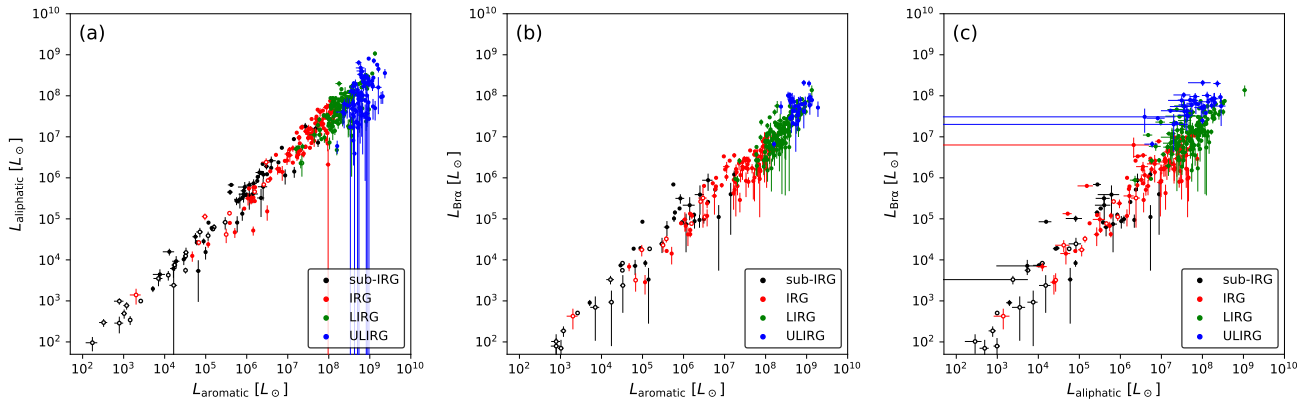


Fig. 5. Scatter plots between (a) $L_{\text{aliphatic}}$ and L_{aromatic} , (b) $L_{\text{Br}\alpha}$ and L_{aromatic} , and (c) $L_{\text{Br}\alpha}$ and $L_{\text{aliphatic}}$ for all the sample galaxies observed with $S/N > 3$ for the detection of the aromatic feature at $3.3 \mu\text{m}$ and with $S/N > 1$ for the detection of the aliphatic features at $3.4\text{--}3.6 \mu\text{m}$ and the H I Br α recombination line for a display purpose: sub-IRGs (black circles), IRGs (red circles), LIRGs (green circles), and ULIRGs (blue circles). The open marks correspond to the results obtained for off-center regions of a galaxy. Alt text: Three scatter plots.

timated from the 456 spectra, from which it is confirmed that those parameters are significantly correlated with each other. Notably, the present study covers as wide a range of L_{aromatic} as about 8 orders of magnitude ($10^2\text{--}10^{10} L_{\odot}$). On the other hand, Kondo et al. (2024) covered a range of $10^6\text{--}10^{10} L_{\odot}$, only about a higher half of the luminosity range covered by the present study.

5.1 Variations in $L_{\text{aliphatic}}/L_{\text{aromatic}}$ from galaxy to galaxy

Figure 6 shows $L_{\text{aliphatic}}/L_{\text{aromatic}}$ plotted against L_{aromatic} for all the sample galaxies. As a reference, we overplot the data points of the Galactic H II regions. As seen in the figure, the values of $L_{\text{aliphatic}}/L_{\text{aromatic}}$ of the sample galaxies are widely distributed from 0.01 to 1, which exhibit considerably large variations, compared to those of the Galactic H II regions. In addition, $L_{\text{aliphatic}}/L_{\text{aromatic}}$ is systematically different across the luminosity classes. The median values of $L_{\text{aliphatic}}/L_{\text{aromatic}}$ for the sub-IRGs, the IRGs, the LIRGs, the ULIRGs, and the Galactic H II regions are 0.43, 0.30, 0.26, 0.15, and 0.26, respectively, and thus the LIRGs show $L_{\text{aliphatic}}/L_{\text{aromatic}}$ values similar to those of the Galactic H II regions. On the other hand, the $L_{\text{aliphatic}}/L_{\text{aromatic}}$ values of the (sub-)IRGs are systematically higher, while the $L_{\text{aliphatic}}/L_{\text{aromatic}}$ values of the ULIRGs are systematically lower than those of the Galactic H II regions. These results imply that the properties of hydrocarbon dust in the (sub-)IRGs and the ULIRGs somewhat differ from those in the LIRGs and the Galactic H II regions.

We plot $L_{\text{aromatic}}/L_{\text{IR}}$, $L_{\text{aliphatic}}/L_{\text{IR}}$, and $L_{\text{aliphatic}}/L_{\text{aromatic}}$ as a function of L_{IR} in figures 7a, 7b, and 7c, respectively. As already pointed out by Kondo et al. (2024), $L_{\text{aromatic}}/L_{\text{IR}}$, $L_{\text{aliphatic}}/L_{\text{IR}}$, and $L_{\text{aliphatic}}/L_{\text{aromatic}}$ decrease with L_{IR} at higher L_{IR} ($> 10^{11} L_{\odot}$). Owing to improved statistics in IRG and sub-IRG sample in the present study, figure 7c shows that $L_{\text{aliphatic}}/L_{\text{aromatic}}$ decreases systematically with L_{IR} over the range of $10^9\text{--}10^{13} L_{\odot}$, while this trend was recognized only at higher L_{IR} ($> 10^{11} L_{\odot}$) in Kondo et al. (2024).

5.2 Relationship between $L_{\text{aliphatic}}/L_{\text{aromatic}}$ and the interstellar radiation field

Mori et al. (2014) and Kondo et al. (2024) showed that $L_{\text{aliphatic}}/L_{\text{aromatic}}$ decreases with the strength of the UV radi-

ation field. Mori et al. (2014) used $I_{\text{cont}, 3.7 \mu\text{m}}/I_{\text{aromatic}}$, which is considered to reflect the ionization degree of PAHs (Haraguchi et al. 2012) and thus as an indicator of the UV radiation field strength. Kondo et al. (2024) used G_0 , which is defined by the far-UV ($6.0\text{--}13.6 \text{ eV}$) radiation field strength normalized to the solar neighborhood value (Habing 1968). In the case of galaxies, the interpretation of $I_{\text{cont}, 3.7 \mu\text{m}}/I_{\text{aromatic}}$ is not straightforward because $I_{\text{cont}, 3.7 \mu\text{m}}$ generally traces not only ionized PAHs but also stellar components. Also, we cannot calculate G_0 for some galaxies, for which we lack the far-IR data needed to derive G_0 from the SED fitting. Therefore, in the present study, we use $L_{\text{Br}\alpha}$ as a tracer of the UV radiation fields, which traces H II regions exposed to extreme-UV radiation ($> 13.6 \text{ eV}$). Figure 8a shows $L_{\text{aliphatic}}/L_{\text{aromatic}}$ as a function of $L_{\text{Br}\alpha}$, where we confirm that both galaxies and Galactic H II regions show gradually decreasing trends with $L_{\text{Br}\alpha}$, which is consistent with the results of Mori et al. (2014) and Kondo et al. (2024).

We also examine the dependence of $L_{\text{aliphatic}}/L_{\text{aromatic}}$ on the radiation hardness. Here we define the hardness by $L_{\text{Br}\alpha}/L_{\text{aromatic}}$ since L_{aromatic} emission is mostly associated with the far-UV while $L_{\text{Br}\alpha}$ with the extreme-UV. As seen in figure 8b, $L_{\text{aliphatic}}/L_{\text{aromatic}}$ globally decreases with $L_{\text{Br}\alpha}/L_{\text{aromatic}}$ and thus the radiation hardness, where there seems to be no systematic difference between the galaxies and the Galactic H II regions. The scatter of the galaxies, however, is considerably larger, and in particular, some of the ULIRGs are largely deviated from the global trend, showing extremely low $L_{\text{aliphatic}}/L_{\text{aromatic}}$ (< 0.1), possible causes of which will be discussed in section 6.4. Hence we cannot explain the variations of $L_{\text{aliphatic}}/L_{\text{aromatic}}$ by the effect of the radiation hardness alone.

6 Discussion

6.1 Robustness of the near-IR fitting results

To check the robustness of the model fitting, we investigate the dependence of the fitting results on the S/N of the fitted data. Based on the typical model spectrum of our sample galaxies with $L_{\text{aliphatic}}/L_{\text{aromatic}} = 0.3$, we generate Gaussian errors with various levels of S/N randomly and add them to the model spectrum. Then, we perform the model fitting to 30000 simulated spectra thus created for a range of $S/N = 1$ to 30 with a step of 0.001. Figure 9 shows $(R_{\text{output}} - R_{\text{input}})/R_{\text{input}}$, where R_{input} is the input

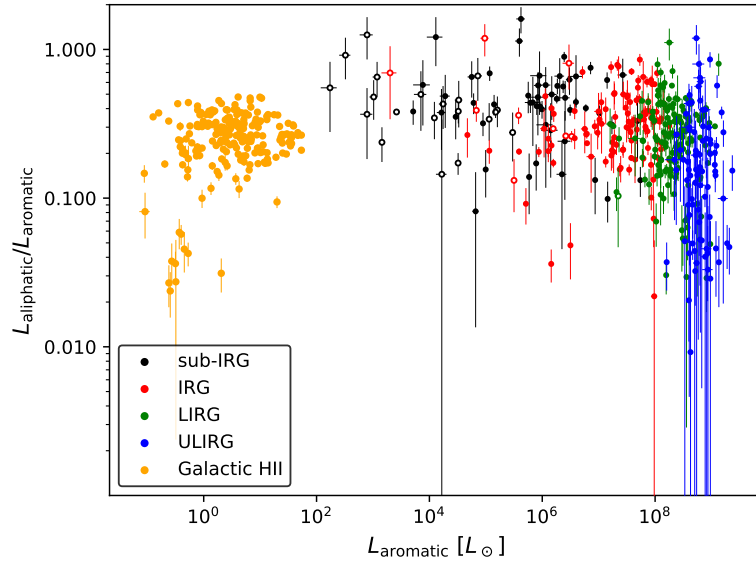


Fig. 6. $L_{\text{aliphatic}}/L_{\text{aromatic}}$ plotted against L_{aromatic} for all the sample galaxies observed with $S/N > 3$ for the detection of the aromatic feature at $3.3 \mu\text{m}$: sub-IRGs (black circles), IRGs (red circles), LIRGs (green circles), ULIRGs (blue circles), and Galactic H II regions (orange circles). The open marks correspond to the results obtained for off-center regions of a galaxy. Alt text: One scatter plot.

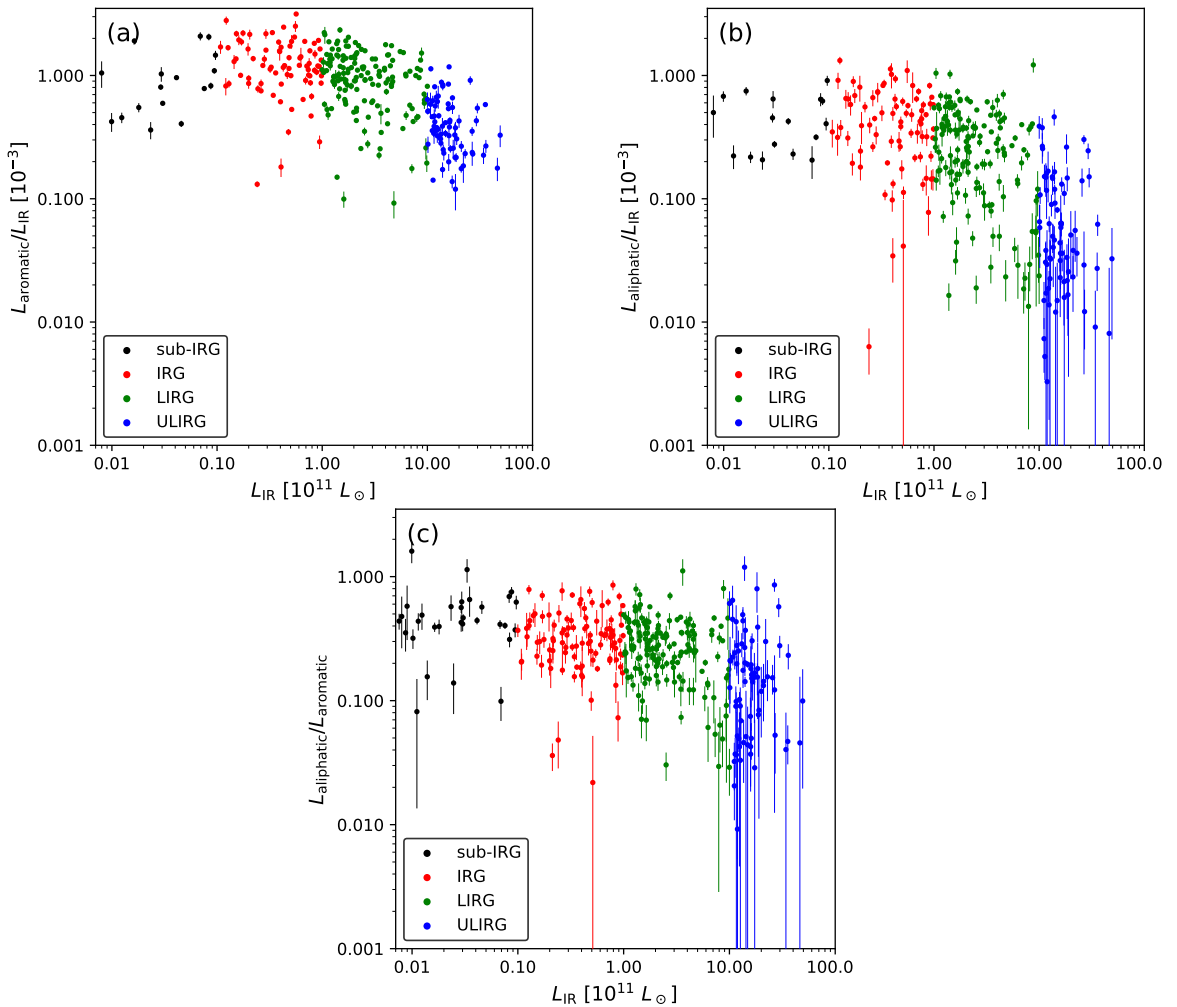


Fig. 7. (a) $L_{\text{aromatic}}/L_{\text{IR}}$, (b) $L_{\text{aliphatic}}/L_{\text{IR}}$, and (c) $L_{\text{aliphatic}}/L_{\text{aromatic}}$ all as a function of L_{IR} for the sample galaxies observed with $S/N > 3$ for the detection of the aromatic feature at $3.3 \mu\text{m}$: sub-IRGs (black circles), IRGs (red circles), LIRGs (green circles), and ULIRGs (blue circles). Alt text: Three scatter plots.

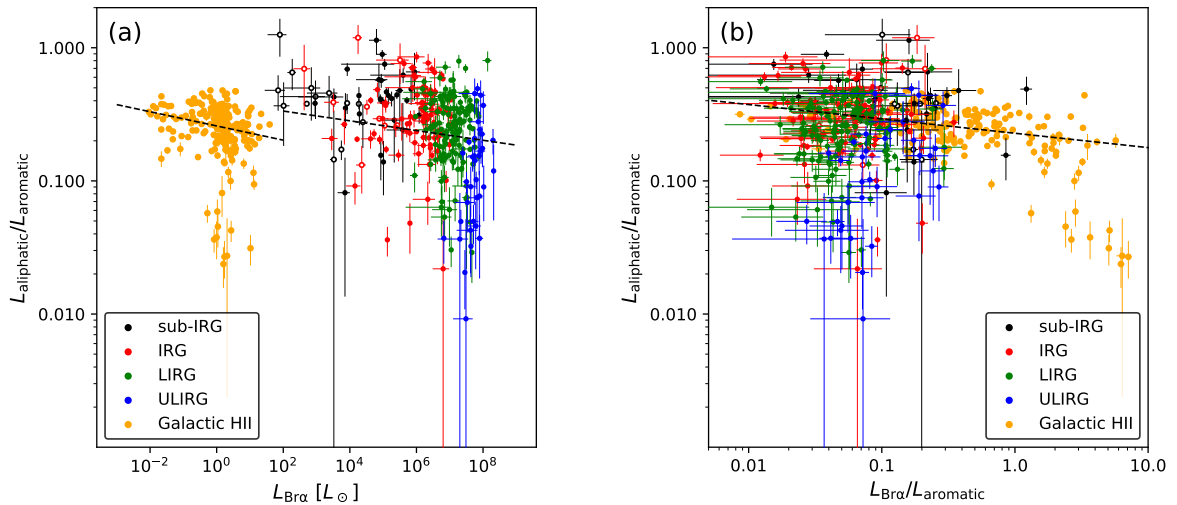


Fig. 8. $L_{\text{aliphatic}}/L_{\text{aromatic}}$ as functions of (a) $L_{\text{Br}\alpha}$ and (b) $L_{\text{Br}\alpha}/L_{\text{aromatic}}$ for all the sample observed with $S/N > 3$ for the detection of the aromatic feature at $3.3 \mu\text{m}$ and with $S/N > 1$ for the detection of the aliphatic features at $3.4\text{--}3.6 \mu\text{m}$ and the H I Br α recombination line for a display purpose: sub-IRG (black circles), IRGs (red circles), LIRGs (green circles), ULIRGs (blue circles), and Galactic H II regions (orange circles). The open marks correspond to the results obtained for off-center regions of a galaxy. The dashed lines in panel(a) are the ones fitted to the sample galaxies and the Galactic H II regions. In contrast, the dashed line in panel(b) is the one fitted to the sample galaxies alone. Alt text: Two scatter plots.

$L_{\text{aliphatic}}/L_{\text{aromatic}}$ value of the model spectrum (i.e., $R_{\text{input}} = 0.3$) and R_{output} is the best-fit value of $L_{\text{aliphatic}}/L_{\text{aromatic}}$, as a function of $I_{\text{aromatic}}/\delta I_{\text{aromatic}}$ estimated from the spectral fitting. Figure 9 indicates that the systematics become significant and the robustness can be lost when $I_{\text{aromatic}}/\delta I_{\text{aromatic}}$ is lower than 5.0. Hence, in the following discussion, we select only the spectral data with the fitting results which satisfy the threshold of $I_{\text{aromatic}}/\delta I_{\text{aromatic}} \geq 5.0$. Figures 10a and 10b are the same as figures 7c and 8b, but only data points with $I_{\text{aromatic}}/\delta I_{\text{aromatic}} \geq 5.0$ are shown, from which we confirm that the trends in figures 7c and 8b do not change significantly with $S/N \geq 5$.

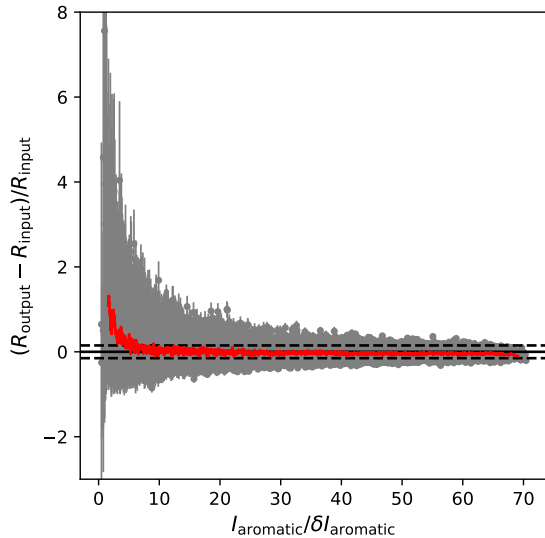


Fig. 9. Dependence of the fitting result of $R_{\text{output}} = L_{\text{aliphatic}}/L_{\text{aromatic}}$ on the S/N based on the simulated spectral data. The red curve shows median values calculated per 51 points along the horizontal axis. The dashed lines represent $(R_{\text{output}} - R_{\text{input}})/R_{\text{input}} = \pm 0.15$. Alt text: One scatter plot.

6.2 Dependence of $L_{\text{aliphatic}}/L_{\text{aromatic}}$ on near-IR continuum properties

First, we investigate whether there is any dependence of $L_{\text{aliphatic}}/L_{\text{aromatic}}$ on $\text{EW}_{\text{aromatic}}$ and Γ , the parameters used for the galaxy classification in section 2.2. Figures 11a and 11b show $L_{\text{aliphatic}}/L_{\text{aromatic}}$ as functions of $\text{EW}_{\text{aromatic}}$ and Γ , respectively, from which we confirm that, for each luminosity class, $L_{\text{aliphatic}}/L_{\text{aromatic}}$ does not have clear dependence on either $\text{EW}_{\text{aromatic}}$ or Γ , only the systematic differences between the different luminosity classes outstanding. Thus the underlying continuum intensity ($\text{EW}_{\text{aromatic}}$) and the $3 \mu\text{m}$ continuum color (Γ) are not important parameters to explain the variations of $L_{\text{aliphatic}}/L_{\text{aromatic}}$.

On the contrary, we find that the $4 \mu\text{m}$ continuum color ($F_{4.2 \mu\text{m}}/F_{3.7 \mu\text{m}}$) is a key parameter, as shown in figure 11c. Not only within each luminosity class but also over all the luminosity range, $L_{\text{aliphatic}}/L_{\text{aromatic}}$ consistently decreases with the $4 \mu\text{m}$ continuum color from blue to red, where the (sub-)IRGs tend to be bluer while the ULIRGs redder at $4 \mu\text{m}$. In the following sections, we discuss what makes the $4 \mu\text{m}$ continuum bluer and $L_{\text{aliphatic}}/L_{\text{aromatic}}$ higher for the (sub-)IRGs, while the $4 \mu\text{m}$ continuum redder and $L_{\text{aliphatic}}/L_{\text{aromatic}}$ lower for the ULIRGs.

6.3 A possible cause for high $L_{\text{aliphatic}}/L_{\text{aromatic}}$ of (sub-)IRGs

Considering that the $4 \mu\text{m}$ bluer continuum is likely to be related with old stellar populations, we utilize L_{star} , which is derived from the SED fitting in section 4, and examine the relationship between $F_{4.2 \mu\text{m}}/F_{3.7 \mu\text{m}}$ and $L_{\text{star}}/L_{\text{IR}}$. As shown in figure 12a, galaxies with higher $L_{\text{star}}/L_{\text{IR}}$ show bluer continuum colors at $4 \mu\text{m}$, which indicates that the $4 \mu\text{m}$ bluer continuum is indeed related to the stellar emission.

The higher $L_{\text{aliphatic}}/L_{\text{aromatic}}$ seen for some of the (sub-)IRGs is caused by either higher $L_{\text{aliphatic}}$ or lower L_{aromatic} (or both). Figure 12b shows the relationship between $L_{\text{aliphatic}}/L_{\text{IR}}$ and $L_{\text{aromatic}}/L_{\text{IR}}$, where we can see that the distributions of the (sub-)IRG samples with $L_{\text{aliphatic}}/L_{\text{aromatic}} > 0.35$

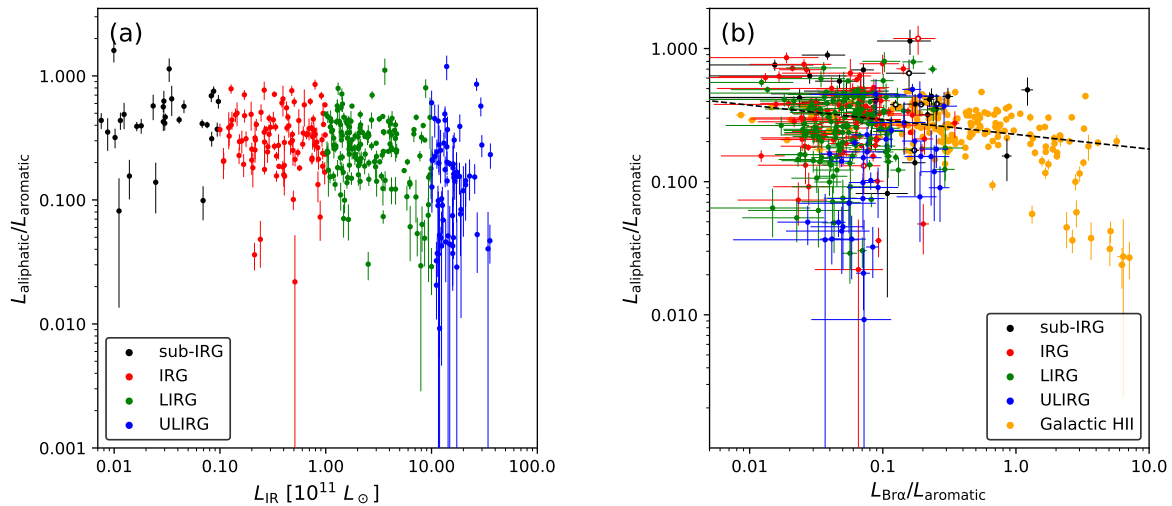


Fig. 10. (a) Same as figure 7c and (b) same as figure 8b, but only data points with $I_{\text{aromatic}}/\delta I_{\text{aromatic}} \geq 5.0$ are shown. Alt text: Two scatter plots.

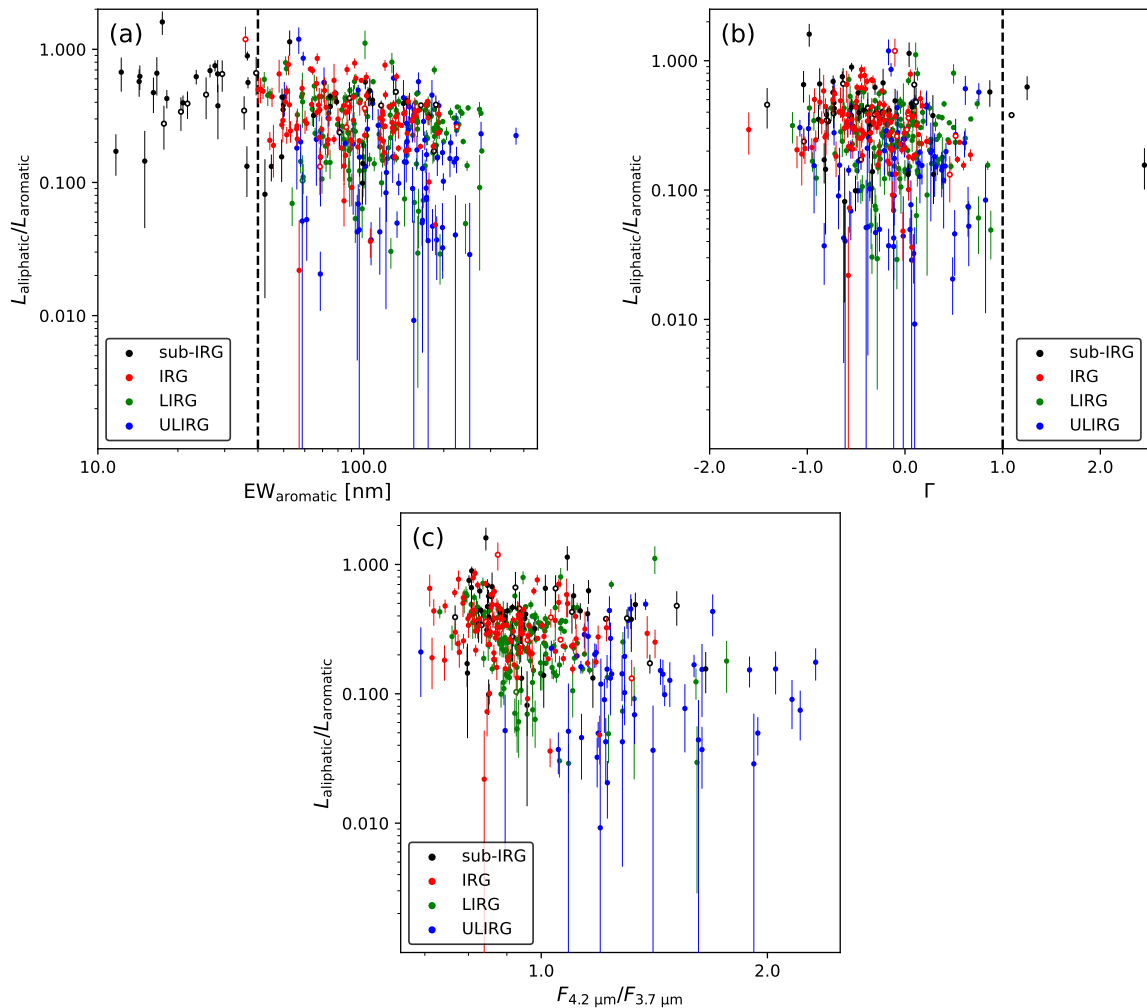


Fig. 11. $L_{\text{aliphatic}}/L_{\text{aromatic}}$ as functions of (a) $\text{EW}_{\text{aromatic}}$, (b) Γ , and (c) $F_{4.2 \mu\text{m}}/F_{3.7 \mu\text{m}}$ for the sample galaxies, color-coded with the luminosity class: sub-IRG (black circles), IRGs (red circles), LIRGs (green circles), and ULIRGs (blue circles). The open marks correspond to the results obtained for off-center regions of a galaxy. The dashed lines in panels(a) and (b) correspond to $\text{EW}_{\text{aromatic}} = 40 \text{ nm}$ and $\Gamma = 1$, respectively, which are used as thresholds to identify the pure star-forming (U)LIRG and IRG samples (i.e., $\text{EW}_{\text{aromatic}} > 40 \text{ nm}$ and $\Gamma < 1$). Alt text: Three scatter plots.

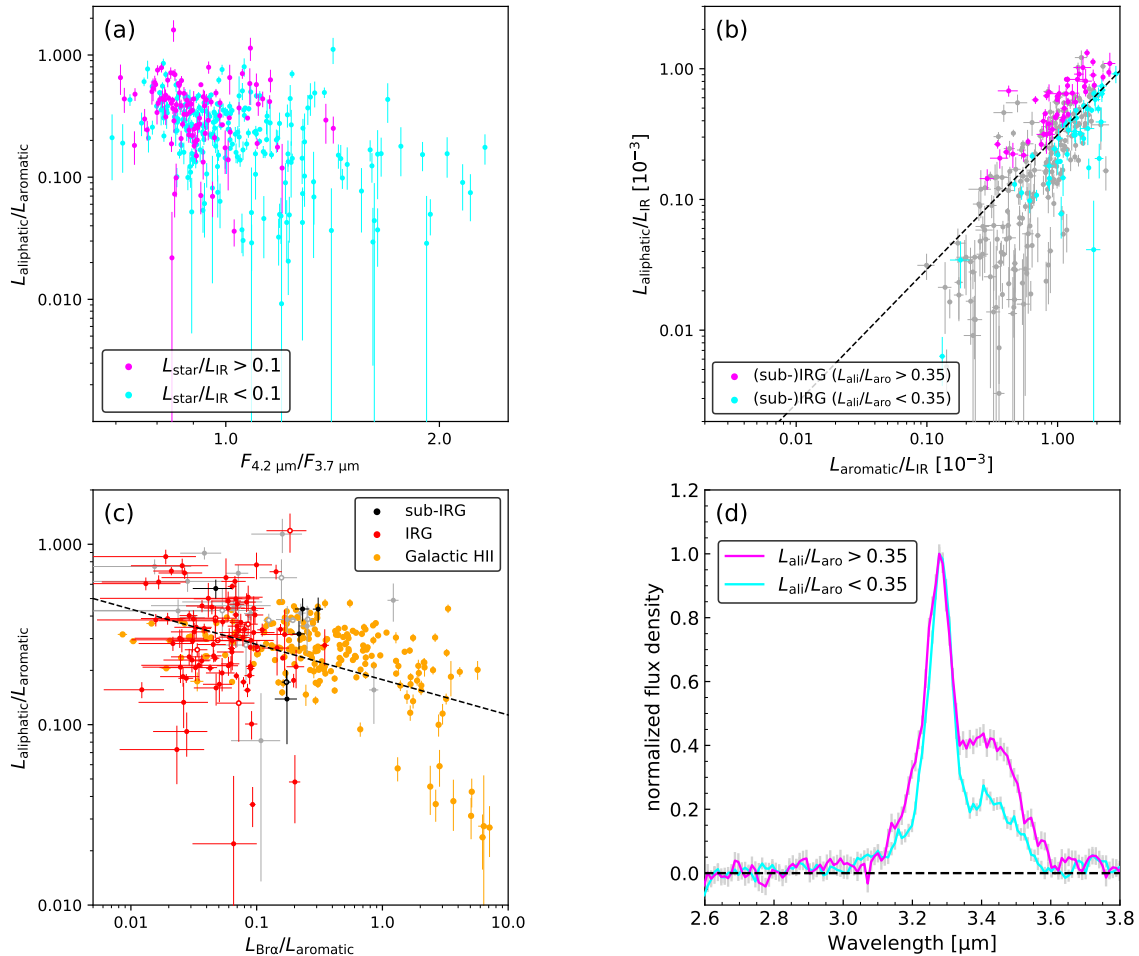


Fig. 12. (a) Same as figure 11c, but color-coded with $L_{\text{star}}/L_{\text{IR}}$: $L_{\text{star}}/L_{\text{IR}} > 0.1$ (magenta circles) and $L_{\text{star}}/L_{\text{IR}} < 0.1$ (cyan circles). (b) Relationship between $L_{\text{aliphatic}}/L_{\text{IR}}$ and $L_{\text{aromatic}}/L_{\text{IR}}$ for the (sub-)IRG samples: $L_{\text{aliphatic}}/L_{\text{aromatic}} > 0.35$ (magenta circles) and $L_{\text{aliphatic}}/L_{\text{aromatic}} < 0.35$ (cyan circles). The (U)LIRG samples are shown in grey color. The dashed line in panel(b) is the one fitted to the (U)LIRGs data points. (c) Same as figure 10b, but plotted only for the (sub-)IRGs and the Galactic H II regions. The grey data points represent sub-IRGs which are reported to have AGNs based on NED or SIMBAD⁴. The dashed line in panel(c) is the one fitted to the non-AGN (sub-)IRGs data points. (d) The stacked spectra of the aromatic and aliphatic features of the (sub-)IRG sample, where the H_2O ice absorption is corrected and the continuum is subtracted (see equation (1) in text). Alt text: Three scatter plots and one graph.

and $L_{\text{aliphatic}}/L_{\text{aromatic}} < 0.35$ are separated along the vertical ($L_{\text{aliphatic}}/L_{\text{IR}}$) axis more clearly than along the horizontal ($L_{\text{aromatic}}/L_{\text{IR}}$) axis. Thus (sub-)IRGs with high $L_{\text{aliphatic}}/L_{\text{aromatic}}$ are likely to be caused by high $L_{\text{aliphatic}}$, but not by low L_{aromatic} .

Then we revisit the result of figure 10b, $L_{\text{aliphatic}}/L_{\text{aromatic}}$ as a function of the UV radiation hardness. In figure 12c, we plot only star-forming (sub-)IRGs together with the Galactic H II regions, where we can recognize a global decreasing trend more clearly. Hence, relatively high $L_{\text{aliphatic}}$ is probably connected to the softer UV radiation, which is consistent with the large old stellar population (i.e., high $L_{\text{star}}/L_{\text{IR}}$). Since aliphatic hydrocarbons are more fragile than aromatic hydrocarbons for photodissociation, a relatively high abundance of aliphatic hydrocarbons is likely to reflect the intrinsic nature of PAHs outside the H II region where the PAHs are not irradiated by strong UV radiation fields and thus remain non-processed. In figure 12d, we show the stacked spectra of the aromatic and aliphatic features of the (sub-)IRG sample, which may exhibit the authentic spectral features of UV-non-processed PAHs rich with aliphatic side groups as a form

of the evolution of interstellar organic matter in galaxies.

6.4 Possible causes for low $L_{\text{aliphatic}}/L_{\text{aromatic}}$ of ULIRGs

As shown in figure 11c, the extremely low $L_{\text{aliphatic}}/L_{\text{aromatic}}$ for some ULIRGs is clearly related to the red continuum at $4 \mu\text{m}$ and thus most probably the presence of a hot dust component. Then we utilize L_{hot} , which is derived from the SED fitting, and examine the relationship between $F_{4.2 \mu\text{m}}/F_{3.7 \mu\text{m}}$ and $L_{\text{hot}}/L_{\text{IR}}$. As seen in figure 13a, galaxies with higher $L_{\text{hot}}/L_{\text{IR}}$ show redder continuum colors at $4 \mu\text{m}$, which indicates that the $4 \mu\text{m}$ redder continuum is indeed related to the hot dust emission. A possibility of the origin of the hot dust component is AGNs, which escape our removal of AGN candidates from the ULIRG sample based on the near-IR spectra ($\text{EW}_{\text{aromatic}}$ and Γ). For instance, galaxies with compact obscured nuclei (CONs; Falstad et al. 2021) can show continuum colors red at $4 \mu\text{m}$ but relatively blue at $3 \mu\text{m}$ (i.e., $\Gamma < 1$). Another possibility is a galaxy merger, which can enhance starburst through the interaction of galaxies, producing hot

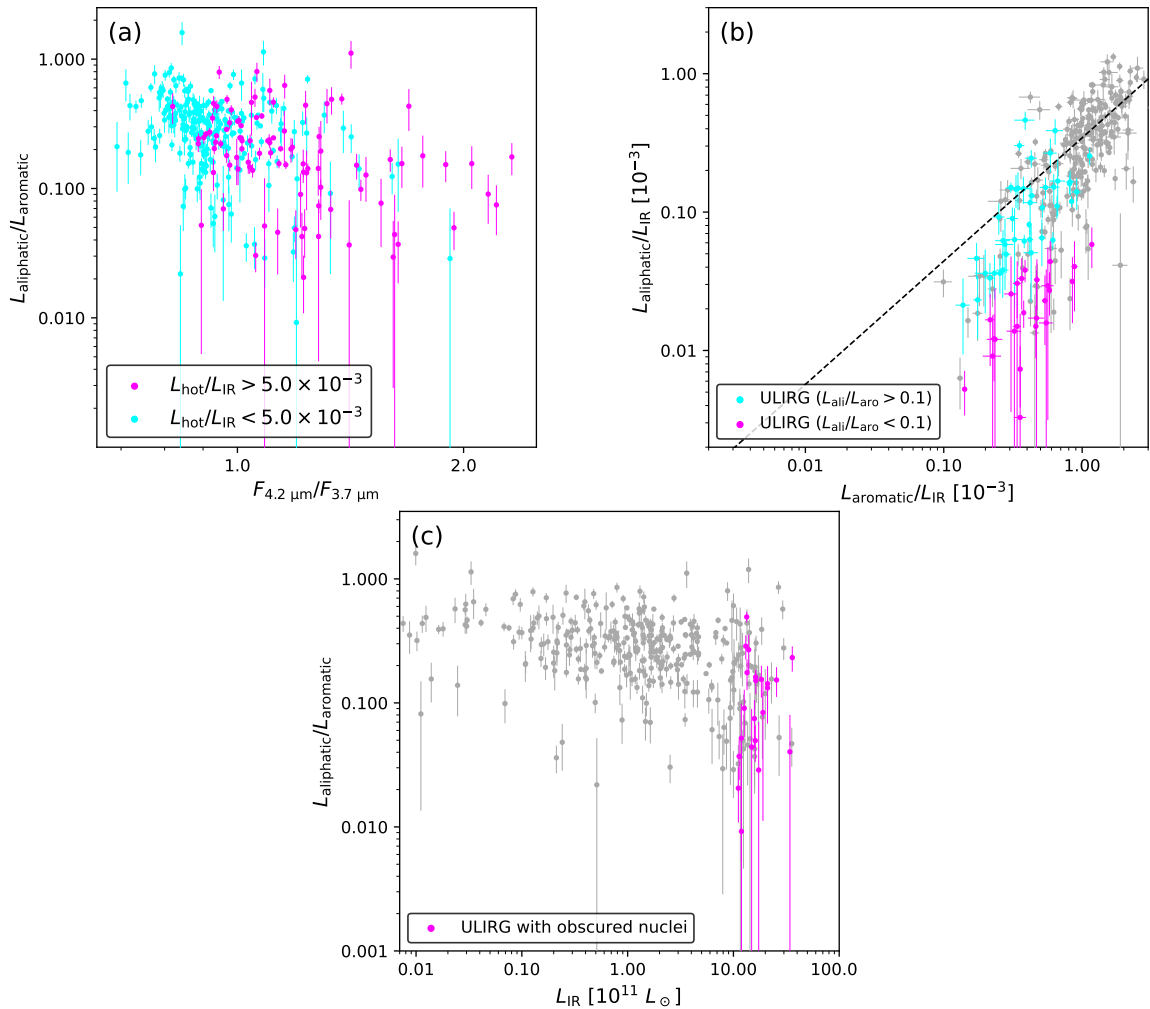


Fig. 13. (a) Same as figure 11c, but color-coded with $L_{\text{hot}}/L_{\text{IR}}$: $L_{\text{hot}}/L_{\text{IR}} > 5.0 \times 10^{-3}$ (magenta circles) and $L_{\text{hot}}/L_{\text{IR}} < 5.0 \times 10^{-3}$ (cyan circles). (b) Same as figure 12b, but for ULIRG sample: $L_{\text{aliphatic}}/L_{\text{aromatic}} < 0.1$ (magenta circles) and $L_{\text{aliphatic}}/L_{\text{aromatic}} > 0.1$ (cyan circles). The (sub)IRG and LIRG samples are shown in grey color. The dashed line in panel(b) is the one fitted to the (sub-)IRG and LIRG data points. (c) Same as figure 10a, but ULIRGs with obscured nuclei based on the Spitzer/IRS mid-IR spectra (Tsuchikawa et al. 2021; Donnan et al. 2023) are denoted by magenta circles, while the others by grey circles. Alt text: Three scatter plots.

dust components. In line with this, Kondo et al. (2024) suggested that in addition to the ISRF strength, galaxy mergers with strong shocks may cause a further decrease in $L_{\text{aliphatic}}/L_{\text{aromatic}}$. On the contrary, Smith et al. (2007) pointed out that such hot dust as heated by the enhanced starburst cannot account for the continuum reddening at $4 \mu\text{m}$. Moreover, Lyu et al. (2025) showed that galaxy mergers do not decrease $L_{\text{aliphatic}}/L_{\text{aromatic}}$ clearly using their JWST sample, although the luminosity classes of the galaxies are much different between our sample and their sample as shown in figure 2.

In the same manner as in the previous subsection, the extremely low $L_{\text{aliphatic}}/L_{\text{aromatic}} (< 0.1)$ seen for some of the ULIRGs is caused by either lower $L_{\text{aliphatic}}$ or higher L_{aromatic} (or both). Figure 13b is the same as figure 12b, but we focus on the ULIRG sample, where we can see that their distributions with $L_{\text{aliphatic}}/L_{\text{aromatic}} > 0.1$ and $L_{\text{aliphatic}}/L_{\text{aromatic}} < 0.1$ are separated along the vertical ($L_{\text{aliphatic}}/L_{\text{IR}}$) axis more clearly than along the horizontal ($L_{\text{aromatic}}/L_{\text{IR}}$) axis. Thus ULIRGs with extremely low $L_{\text{aliphatic}}/L_{\text{aromatic}}$ are likely to be caused by low $L_{\text{aliphatic}}$, but not by high L_{aromatic} .

Past studies reported that some IR galaxies in merger systems

show both starburst and AGN activities (e.g., Arp 299: Ballo et al. 2004; Mrk 273: Nardini et al. 2008, 2009; NGC 3341: Bianchi et al. 2013; Mrk 266: Beaulieu et al. 2023; NGC 3256: Bohn et al. 2024; NGC 6240: Hermosa Muñoz et al. 2025). The galactic nuclei in these merger systems are often heavily obscured, for which aliphatic hydrocarbon features are observed in the absorption at $3.4 \mu\text{m}$ (e.g., Imanishi et al. 2008, 2010). Consequently, the observed $L_{\text{aliphatic}}/L_{\text{IR}}$ in ULIRGs that associate heavily obscured nuclei is likely to be underestimated, because the aliphatic emission features are blended with the aliphatic absorption features. Indeed, 33% of the ULIRGs in our sample are likely to contain obscured nuclei, based on the Spitzer/IRS mid-IR spectra (Tsuchikawa et al. 2021; Donnan et al. 2023). Figure 13c shows the distribution of such ULIRGs in the $L_{\text{aliphatic}}/L_{\text{aromatic}}$ vs L_{IR} plane, from which we recognize that there is an indication of ULIRGs with obscured nuclei showing extremely low $L_{\text{aliphatic}}/L_{\text{aromatic}}$. To correctly estimate $L_{\text{aliphatic}}/L_{\text{aromatic}}$ in merger galaxies with heavily obscured nuclei, it is necessary to consider modeling both aliphatic emission and absorption features for each interacting galaxy with higher spatial and spectral resolutions spectra such as those taken with JWST/NIRSpec.

7 Conclusions

Using near-IR (2.55–4.85 μm) spectra of nearby galaxies obtained with AKARI/IRC, we have systematically investigated the relationship between the luminosities of the aromatic hydrocarbon feature at 3.3 μm (L_{aromatic}) and the aliphatic hydrocarbon features at 3.4–3.6 μm ($L_{\text{aliphatic}}$) for 243 spectra of 240 star-forming (U)LIRGs, 119 spectra of 105 star-forming IRGs, and 94 spectra of 65 sub-IRGs, in addition to 232 spectra of 36 Galactic H II regions as a reference sample. As a result, $L_{\text{aliphatic}}/L_{\text{aromatic}}$ of the sample galaxies shows considerably large variations, compared to the Galactic H II regions, where $L_{\text{aliphatic}}/L_{\text{aromatic}}$ decreases systematically with the total infrared luminosity over the range of 10^9 – 10^{13} L_{\odot} . We find that (sub-)IRGs with continuum colors bluer at 4 μm tend to have higher $L_{\text{aliphatic}}/L_{\text{aromatic}}$, while ULIRGs with continuum colors redder at 4 μm tend to have extremely low $L_{\text{aliphatic}}/L_{\text{aromatic}}$. We show that the variations of $L_{\text{aliphatic}}/L_{\text{aromatic}}$ are mainly caused by the changes in $L_{\text{aliphatic}}$ but not by those in L_{aromatic} . It is probable that the (sub-)IRGs with high $L_{\text{aliphatic}}/L_{\text{aromatic}}$ are relatively inactive with star formation, having aliphatic-rich hydrocarbon dust, while the ULIRGs with extremely low $L_{\text{aliphatic}}/L_{\text{aromatic}}$ are merger systems with galactic nuclei, showing very low $L_{\text{aliphatic}}$. We conclude that the former is likely to reflect the intrinsic nature of PAHs outside the H II region where the PAHs remain non-processed by strong UV radiation fields, while the latter is likely to be caused by blending aliphatic emission and absorption features due to the presence of an obscured galactic nucleus in merger systems.

Acknowledgments

This research is based on observations with AKARI, a JAXA project with the participation of ESA. This publication makes use of data products from the Wide-field Infrared Survey Explorer, which is a joint project of the University of California, Los Angeles, and the Jet Propulsion Laboratory/California Institute of Technology, funded by the National Aeronautics and Space Administration, and data products from the Infrared Astronomical Satellite (IRAS), which is a joint project of the US, UK, and the Netherlands. This research has made use of the NASA/IPAC Extragalactic Database, which is funded by the National Aeronautics and Space Administration and operated by the California Institute of Technology and use of the SIMBAD database, operated at CDS, Strasbourg, France. This work is financially supported by JST SPRING, Grant Number JPMJSP2125. The principal author is grateful for the ‘‘THERS Make New Standards Program for the Next Generation Researchers.’’ This work was supported by JSPS KAKENHI Grant Number 24K07094.

References

Ballo, L., Braitto, V., Della Ceca, R., Maraschi, L., Tavecchio, F., & Dadina, M. 2004, *ApJ*, 600, 2, 634.
 Beaulieu, D., Petric, A., Robert, C., Alatalo, K., Heckman, T., Merhi, M., Rousseau-Nepton, L., & Rowlands, K. 2023, *MNRAS*, 518, 1, 1407.
 Berné, O., & Tielens, A. G. G. M. 2012, *Proceedings of the National Academy of Science*, 109, 401.
 Bianchi, S., Piconcelli, E., Pérez-Torres, M. Á., Fiore, F., La Franca, F., Mathur, S., & Matt, G. 2013, *MNRAS*, 435, 3, 2335.
 Bohn, T., et al. 2024, *ApJ*, 977, 1, 36.
 Compiègne, M., et al. 2011, *A&A*, 525, A103.
 Doi, Y., et al. 2015, *PASJ*, 67, 3, 50.

Donnan, F. R., et al. 2023, *A&A*, 669, A87.
 Draine, B. T. 2011, *Physics of the Interstellar and Intergalactic Medium* (Princeton, New Jersey: Princeton University Press).
 Draine, B. T., & Li, A. 2007, *ApJ*, 657, 810.
 Egorov, O. V., et al. 2023, *ApJL*, 944, 2, L16.
 Engelbracht, C. W., et al. 2004, *ApJS*, 154, 1, 248.
 Falstad, N., et al. 2021, *A&A*, 649, A105.
 Galliano, F., Madden, S. C., Tielens, A. G. G. M., Peeters, E., & Jones, A. P. 2008, *ApJ*, 679, 310.
 García-Bernete, I., et al. 2025, *A&A*, 696, A135.
 Habing, H. J. 1968, *Bull. Astron. Inst. Netherlands*, 19, 421.
 Haraguchi, K., Nagayama, T., Kurita, M., Kino, M., & Sato, S. 2012, *PASJ*, 64, 127.
 Hemachandra, D., et al. 2015, *MNRAS*, 454, 818.
 Hermosa Muñoz, L., et al. 2025, *A&A*, 693, A321.
 Hummer, D. G., & Storey, P. J. 1987, *MNRAS*, 224, 801.
 Imanishi, M., Nakagawa, T., Ohshima, Y., Shirahata, M., Wada, T., Onaka, T., & Oi, N., 2008, *PASJ*, 60, S489.
 Imanishi, M., Nakagawa, T., Shirahata, M., Ohshima, Y., & Onaka, T. 2010, *ApJ*, 721, 1233.
 Ishihara, D., et al. 2010, *A&A*, 514, A1.
 Kaneda, H., Onaka, T., Sakon, I., Kitayama, T., Okada, Y., & Suzuki, T. 2008, *ApJ*, 684, 270.
 Katayama, R., Kaneda, H., Kokusho, T., Kondo, T., Oyabu, S., Suzuki, T., & Tsuchikawa, T. 2025, *A&A*, 703, A179.
 Kennicutt, R. C., et al. 2011, *PASP*, 123, 910, 1347.
 Kondo, T., Kondo, A., Murata, K. L., Kokusho, T., Oyabu, S., Suzuki, T., Katayama, R., & Kaneda, H. 2024, *PASJ*, 76, 5, 1041.
 Kwok, S. 2007, *Physics and Chemistry of the Interstellar Medium* (Sausalito, California: University Science Books).
 Kwok, S. 2011, *Organic Matter in the Universe* (Weinheim, Germany: Wiley-VCH).
 Lai, T. S.-Y., et al. 2023, *ApJL*, 957, L26.
 Li, A. 2020, *Nature Astronomy*, 4, 339.
 Lyu, J., Yang, X., Li, A., Sun, F., Rieke, G. H., Alberts, S., & Shivaee, I. 2025, *ApJ*, 986, 2, 156.
 Mori, T. I., Onaka, T., Sakon, I., Ishihara, D., Shimonishi, T., Ohsawa, R., & Bell, A. C. 2014, *ApJ*, 784, 53.
 Moshir, M., et al. 1990, *BAAS*, 22, 1325.
 Murakami, H., et al. 2007, *PASJ*, 59, S369.
 Nardini, E., Risaliti, G., Salvati, M., Sani, E., Imanishi, M., Marconi, A., & Maiolino, R. 2008, *MNRAS*, 385, 1, L130.
 Nardini, E., Risaliti, G., Salvati, M., Sani, E., Watabe, Y., Marconi, A., & Maiolino, R. 2009, *MNRAS*, 399, 3, 1373.
 Ohshima, Y., et al. 2007, *PASJ*, 59, S411.
 Onaka, T., et al. 2007, *PASJ*, 59, S401.
 Peeters, E., Hony, S., Van Kerckhoven, C., Tielens, A. G. G. M., Allamandola, L. J., Hudgins, D. M., & Bauschlicher, C. W. 2002, *A&A*, 390, 1089.
 Persic, M. & Rephaeli, Y. 2019, *MNRAS*, 490, 2, 1489.
 Persic, M., Rephaeli, Y., & Rando, R. 2024, *A&A*, 685, A47.
 Sanders, D. B. & Mirabel, I. F. 1996, *ARA&A*, 34, 749.
 Shimonishi, T., Onaka, T., Kato, D., Sakon, I., Ita, Y., Kawamura, A., & Kaneda, H. 2010, *A&A*, 514, A12.
 Sloan, G. C., Bregman, J. D., Geballe, T. R., Allamandola, L. J., & Woodward, E. 1997, *ApJ*, 474, 2, 735.
 Smith, B. J., Struck, C., Hancock, M., Appleton, P. N., Charmandaris, V., & Reach, W. T. 2007, *AJ*, 133, 3, 791.
 Suzuki, T., Kaneda, H., & Onaka, T. 2013, *A&A*, 554, A8.
 Tielens, A. G. G. M. 2008, *ARA&A*, 46, 289.
 Tsuchikawa, T., Kaneda, H., Oyabu, S., Kokusho, T., Kobayashi, H., Yamagishi, M., & Toba, Y. 2021, *A&A*, 651, A117.
 Wright, E. L., et al. 2010, *AJ*, 140, 1868.
 Yamagishi, M., Kaneda, H., Ishihara, D., Kondo, T., Onaka, T., Suzuki, T., & Minh, Y. C. 2012, *A&A*, 541, A10.
 Yamagishi, M., Kaneda, H., Ishihara, D., Oyabu, S., Onaka, T., Shimonishi, T., & Suzuki, T. 2011, *ApJL*, 731, 1, L20.
 Zhang, Z.-Y., Gao, Y., Henkel, C., Zhao, Y., Wang, J., Menten, K. M., &

Güsten, R. 2014, *ApJL*, 784, 2, L31.